Supporting Information

Three-dimensional and time-ordered SERS hotspot matrix

Honglin Liu,[1] Zhilin Yang,[2] Lingyan Meng,[2] Yudie Sun,[1] Jie Wang,[3] Liangbao Yang,[1] Jinhuai Liu,[1] and Zhongqun Tian[2]

1 Institute of Intelligent Machines, Chinese Academy of Sciences, Hefei 230031, China

2 State Key Laboratory of Physical Chemistry of Solid Surfaces and College of Chemistry and Chemical Engineering, Xiamen University, Xiamen 361005, China

3 Shanghai Synchrotron Radiation Facility, Shanghai Institute of Applied Physics, Chinese Academy of Sciences, Shanghai 201204, China

S1. Supplementary methods

S1.1. Chemical materials and experimental setups

The $AgNO_3$, sodium citrate, R6G, PATP, NP, MPY, and Paraoxon used in the experiment were all of analytical grade (≥99.8%), purchased from Sinopharm Chemical Reagent Co., Ltd., (Shanghai, China) and used as received without further purification. Ultrapure water (>18.0 MΩ·cm) was prepared using a Millipore Milli-Q gradient system throughout the experiment. The MAMP and MDMA-HCl were gifts from the Beijing Institute of Pharmacology and Toxicology (Academy of Military Medical Sciences, Beijing, China) and were also of analytical grade.

SR-SAXS measurements were performed at the μSpot beamline BL16B1 at SSRF (Shanghai, China). The focusing scheme of the beamline is designed to provide a divergence of 0.4 mrad (horizontally and vertically) and a beam diameter of ~200 μm with a maximal photon flux of 2×10^{13} photons/(s.10^{-3}BW) at 8.1 keV. SAXS is a common method of determining the shape and size of particles in solution. The scattering signal originates from the contrast between the nanoparticles and the solvent or air. When evaluating SAXS curves, it is common to use model curves to fit the experimental scattering curves. The SAXS data were processed using the Fit2d and Irena software packages, the latter of which provides a detailed review of the topic[1].

Dark-field spectrum measurements were conducted using an inverted microscope (eclipse Ti-U, Nikon, Japan) equipped with a dark-field condenser (0.8 < NA < 0.95) and a 40x objective lens (NA = 0.8), which was provided by Prof. Long's group (East China University of Science and Technology, Shanghai). A 100-W halogen lamp provided white light to excite the NPs and generate plasmon resonance scattering light. The dark-field color images were acquired using a true-color digital camera (Nikon DS-fi).

For in situ micro-UV measurements, the droplet to be measured was placed on a transparent fluorosilylated quartz slide, which was then placed on the top of an optics-integrating sphere. An aluminized mirror was then used to reflect the incident light back to the optics-integrating sphere. The light from the integrating sphere passed through the sample twice and then returned to the sphere. The light and sample backgrounds could be deducted easily and simultaneously. The time-resolved optical behavior of the colloids could be precisely followed with a maximum time resolution of 10 s.

S1.2. Synthesis and characterization of Ag sols

The Ag sols were prepared in accordance with the method of Lee and Meisel.[2] In brief, 1 ml of 0.1 M $AgNO_3$ was added to 99 ml of Milli-Q water (18.2 MΩ), purged with pure N_2, and heated to 100 °C; 4 ml of 1% sodium citrate, purged with N_2, was added to the boiling solution under vigorous stirring. The solution was kept boiling for ~1 h. This procedure resulted in a gray-yellow solution with a UV-Vis absorption maximum at 415 nm (Figure S1). The SEM image revealed a distribution of sizes (approximately 40-60 nm), and the mean particle size was approximately 50 nm in diameter. The as-prepared colloid concentration was estimated to be ≈10^{11} colloids/ml or, equivalently, ≈0.17 nM[3]. The Ag sols were first washed once; centrifugation of 1000 μl of Ag sols at 13,000 g for 3 min was then performed, and 995 μl of the colorless supernatant was discarded. The remaining 5 μl, which

contained a black pellet, was re-dispersed under sonication and used as the SERS substrate.

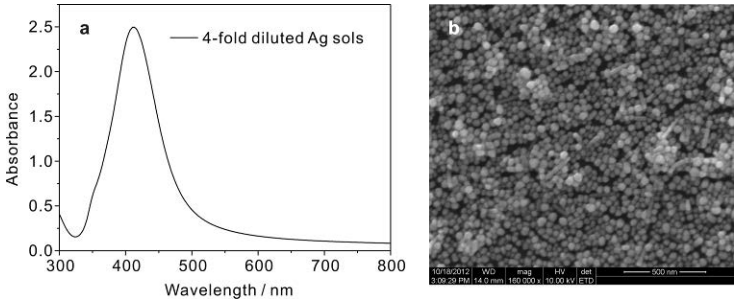

Figure S1. (**a**) UV-Vis absorption spectrum and (**b**) SEM image of the 4-fold-diluted Ag sols.

S1.3. Preparation of extremely dilute solutions

Because a few molecules of R6G can produce distinct SERS signals, great care was required to prepare extremely dilute solutions[4]. The extremely dilute solutions were prepared carefully in accordance with methods described in the literature[4]. First, all glassware was cleaned using a repeated chemical treatment with concentrated HNO_3/HCl (1v3) and was washed with Milli-Q water. The glassware was then baked at 350 °C for 12 h to completely remove any adsorbed organic molecules. For R6G, 5 μl of 1.0 μM R6G was dissolved in 1,000 μl of water to produce a 5-nM R6G solution, followed by 10-fold serial dilutions using 100 μl of this solution diluted with 900 μl of water[4]. The preparation of all other samples followed the above procedures.

S1.4. Hydrophobic treatment

First, the silicon wafer was cleaned and hydroxylated via immersion in a boiling piranha solution (a mixture of 98% H_2SO_4 and 30% H_2O_2, 7:3, v/v) for ~1 h, followed by extensive rinsing with Milli-Q water and drying under a stream of nitrogen. Second, the hydroxylated substrate was immersed in a solution of 40-mM triethoxy-1H,1H,2H,2H-tridecafluoro-n-octylsilane for 2 h. Finally, the glass was rinsed with ethanol and Milli-Q water and then dried under a stream of nitrogen. The surface of this fluorosilylated silicon wafer was hydrophobic. The hydroxylated silicon wafer was hydrophilic and was used as the control.

S1.5. SERS experiments and data processing

As illustrated in Fig. 1b-III, a fluorosilylated silicon wafer was placed on the horizontal X-Y-Z sample stage. A sample droplet was placed on the surface of the silicon wafer. The laser spot was focused on the substrate surface and centered at the top point of this droplet. Time-course SERS mapping was then performed. For all SERS spectra, baseline correction was performed using the LabSpec V5.58.25 software, and the peak frequency and FWHM were obtained from peak fitting.

S2. Adsorbing behaviors of citrate-Ag sols on a hydrophobic-treated silicon wafer

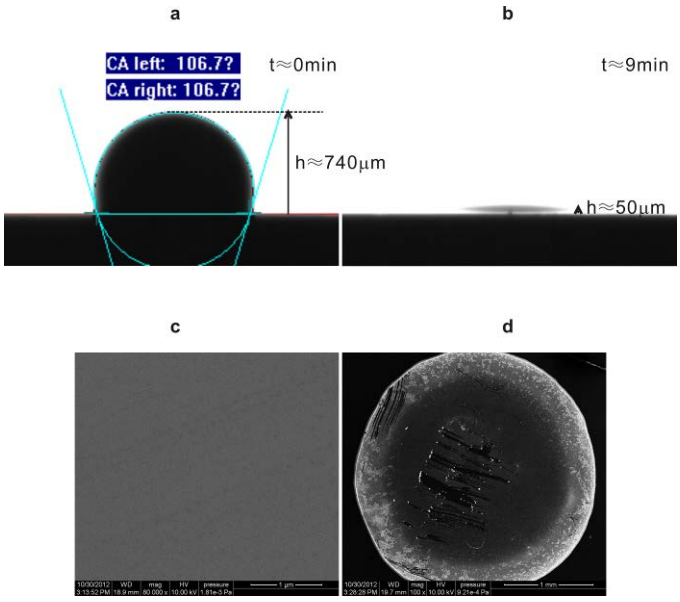

Figure S2. a, Measured contact angle of a 1-μL droplet of concentrated Ag sols on a fluorosilylated silicon wafer. **b**, Remaining portion of the evaporating droplet after approximately 9 min; the height (*h*) had decreased to ~50 μm. **c**, Absorbent paper was used to remove the remaining droplet at approximately 9 min, as shown in **b**, and the surface of the silicon wafer was examined via SEM. **d**, A control experiment was conducted on a hydrophilic-treated silicon wafer. The results demonstrate that the hydrophobic treatment of the silicon wafer prevented the adsorption of AgNPs.

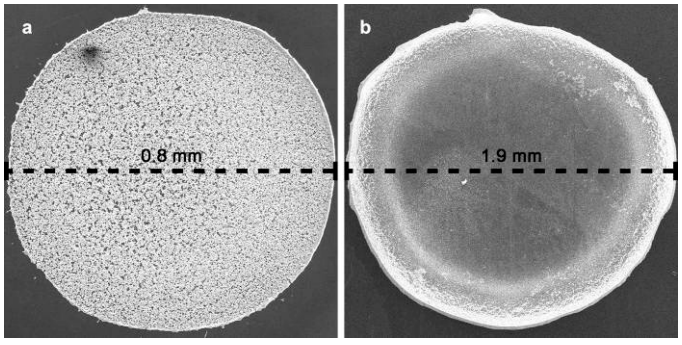

Figure S3. SEM images of the complete deposition of a droplet of concentrated Ag sols on (a) hydrophobic- and (b) hydrophilic-treated silicon wafers. The "coffee ring effect"[5] was greatly weakened on the hydrophobic-treated silicon wafer.

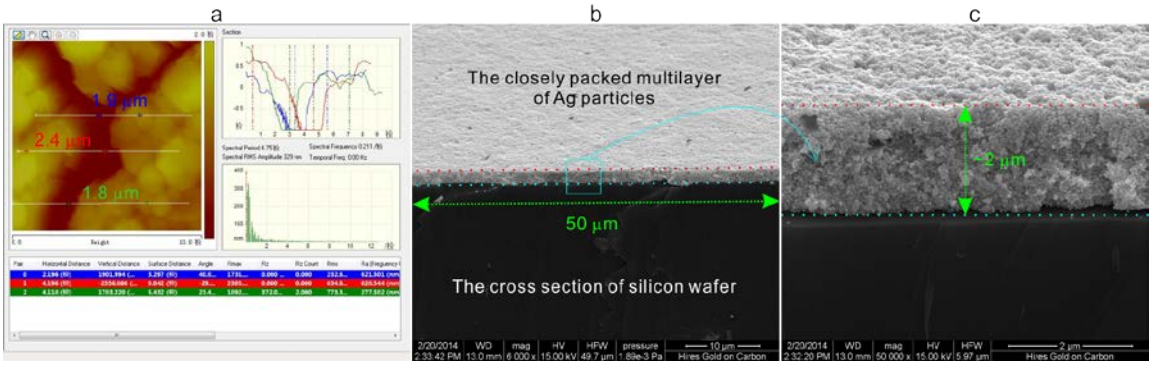

Figure S4. (**a**) AFM and (**b, c**) SEM observations of the height of a closely packed multilayer of Ag nanoparticles. The closely packed particles have a uniform height over a large area.

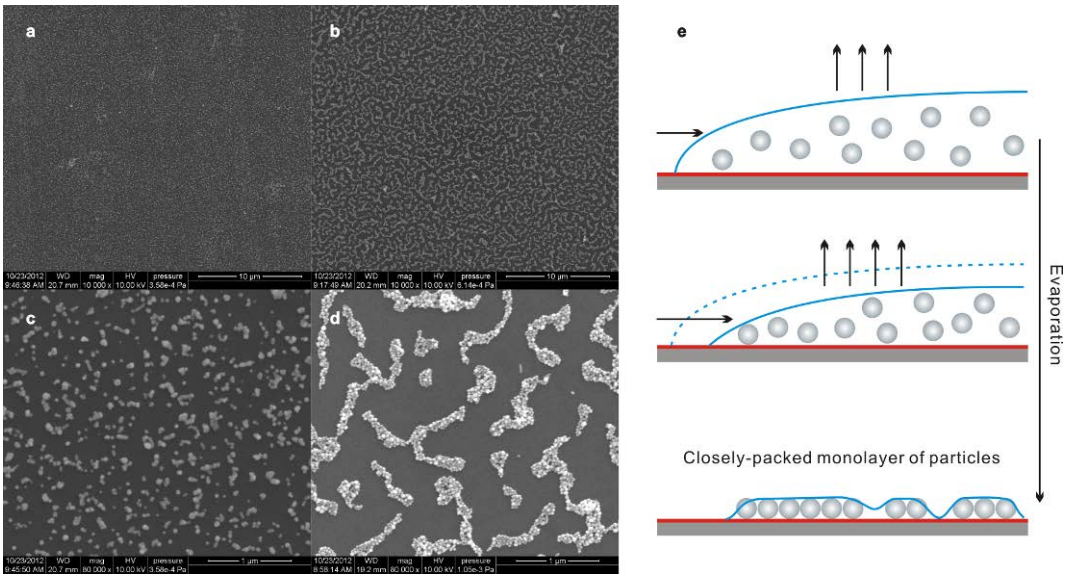

Figure S5. SEM observations of the self-assembly of AgNPs in very dilute sols on (**a**, **c**) hydrophilic- and (**b**, **d**) hydrophobic-treated silicon wafers. The images in c and d are enlarged details of a and b, respectively. (**e**) Schematic illustration of liquid evaporation inducing the formation of a closely packed monolayer array of AgNPs on the hydrophobic-treated surface of a silicon wafer.

S3. Supplementary theoretical analysis

S3.1. Model of the late stage of the water evaporation process

There are four different states of moist agglomerates with decreased liquid-phase content (Figure S6a)[6]. In a droplet of Ag sols, the liquid completely surrounds the particles. During the non-equilibrium evaporation process, the liquid-phase content decreases; therefore, adhesive forces drive the particles closer together, and the average interparticle gap becomes smaller. Air then begins to intersperse into the liquid network, and the particles are held together by adhesive forces at the solid-liquid-air interface, namely, in funicular or pendular states.

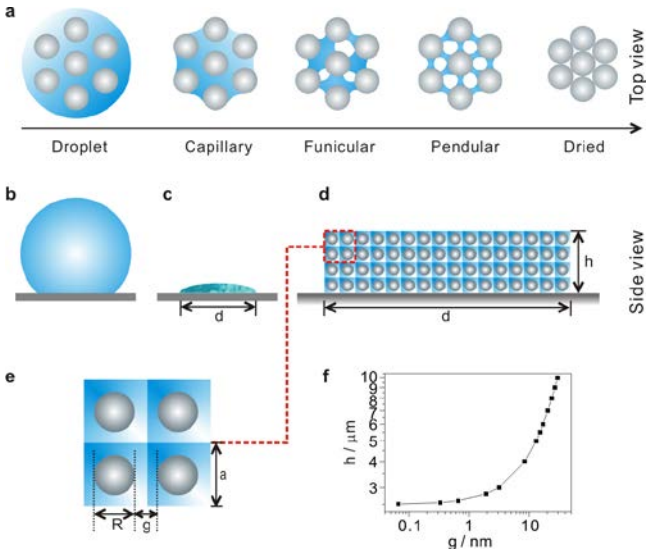

Figure S6. Schematic illustrations of (**a**) the bonding mechanisms for particles in various amounts of liquid, (**b)** the side view of a droplet placed on a hydrophobic-treated silicon surface, and (**c)** the late stage of the evaporation process. **d** and **e**, The late-stage droplet volume is treated as a cylinder, and each Ag particle is surrounded by an imaginary cubic shell of water and uniformly distributed in 3D space. **f**, Calculated relation between the interparticle gap, *g*, and the droplet height, *h*.

In the late stage of water evaporation (Fig. S6c), the diameter (*d*) of the deposition area is much larger than its height (*h*). Hence, we can assume that the deposition volume is a cylinder, all particles are uniformly distributed, and every Ag particle is surrounded by an imaginary cubic shell of water (Figs. S6d and S6e). Thus, the relation between the droplet height and the interparticle gap (Fig. S6f) can be calculated as follows:

$$h = n * a = n * \left(R + g \right) \tag{1}$$

The ionic strength *I* of the droplet of Ag sols in the late stage of water evaporation can be estimated using the following expression:

$$I = f\left(g\right) = I_0 \frac{V_0}{V_g} = \frac{I_0 V_0}{\pi \left(d/2 \right)^2 h} = \frac{I_0 V_0}{\pi \left(d/2 \right)^2 n\left(g + R\right)} \tag{2}$$

Thus, we obtain

$$I_{g=2nm} = I_0 \frac{V_0}{V_{g=2nm}} = \frac{I_0 \times 10^{-9} m^3}{1.281 \times 10^{-12} m^3} = 766 I_0$$

S3.2. Liquid-bridged Ag particles and estimation of the adhesive force

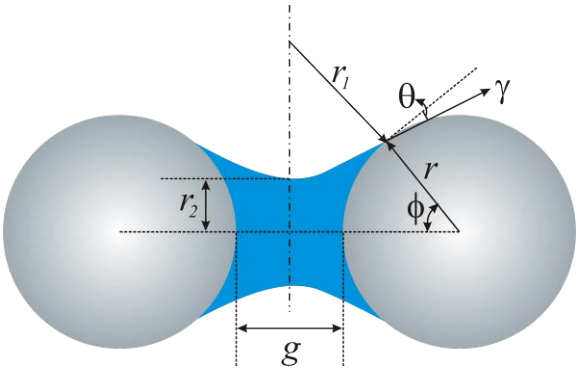

Figure S7. Schematic diagram of a liquid bridge between identical Ag spheres.

The adhesive force in a wet particle medium arises from the surface tension and capillary effects of the liquid. The pressure difference ΔP between the liquid and the air for a meniscus of curvature with radii r_1 and r_2 is given by the Young-Laplace equation as follows:

$$\Delta P = \gamma\left[\frac{1}{r_1}+\frac{1}{r_2}\right] \tag{3}$$

The curvature is positive when the meniscus is drawn back into the liquid phase. When the curvature is positive, ΔP is positive and is often called the suction.

The capillary length

$$L = \sqrt{\frac{2\gamma}{\rho g_0}} \tag{4}$$

provides the length scale for comparison between the capillary force and gravity and is approximately 3.9 mm for water at room temperature. *The capillary force becomes dominant when the relevant length scales are much smaller than L. Hereafter, we consider the situation in which the capillary force is dominant.*

Now let us see how the liquid induces an adhesive force in Ag nanoparticles by considering a liquid bridge between two identical Ag spheres, as shown in Figure S7. The adhesive force between two spheres attributable to the liquid menisci is given by the sum of the surface tension and the suction; the force at the neck of the bridge is estimated as

$$F_{bridge} = 2\pi r_2\gamma + \pi r_2^2\Delta P = 2\pi r\cdot\gamma\sin\phi\left\{\sin\left(\phi+\theta\right)+\frac{r}{2}\sin\phi\left[\frac{1}{r_1}-\frac{1}{r_2}\right]\right\} \tag{5}$$

The surface of a citrate-capped Ag sphere is hydrophilic; therefore, the wetting angle θ is equal to 0. For the special case in which the two spheres are in contact (g = 0),

$$\begin{aligned}&\cos\phi = r/\left(r_1+r\right),\ \tan\phi = \left(r_1+r_2\right)/r\\ &r_1 = r\left(1/\cos\phi-1\right),\ r_2 = r\tan\phi - r_1 = r\left(\tan\phi-1/\cos\phi+1\right)\end{aligned} \tag{6}$$

Hence, we obtain from Eq. 3 that

$$F_{bridge} = \frac{2\pi r\gamma}{1+\tan(\phi/2)} \quad (7)$$

In our experiments, the Ag sphere diameter was ~50 nm, and the density of Ag is 10.5×10^3 kg/m^3; thus, the gravity of each Ag sphere was ~6.73×10^{-18} N, and the γ value of the water was 78.2 mN/m. The calculated adhesive force is between 1.23×10^{-8} N and 6.15×10^{-9} N, assuming that φ is in the range of 0-90°. Hence, *the adhesive force between Ag spheres is far greater than the gravity of Ag spheres.* Moreover, the adhesive force F and the number of liquid bridges k per particle both depend on the liquid content in general, which should also affect the cohesive stress. Recent experiments have demonstrated that k increases very rapidly with increasing liquid content for low liquid content and then saturates.

S3.3. Estimation of particle-particle interaction energy profiles

Table 1 Different types of interparticle forces in citrate-AgNPs[7].

Type of Interaction	**Other Names (Subclasses)**	**Attractive or Repulsive**	**Special Features (and Whether a Body or Surface Force)**
Van der Waals	Dispersion, dipole-induced-dipole, charge-fluctuation, ion-correlation	Attractive between particles	Weak but ubiquitous body force. Force can change sign at some finite distance.
Electrostatic	Coulomb, ionic, salt-bridge, dipolar, hydrogen-bonding, charge-transfer (harpooning), double-layer	Repulsive between charges	Strong, long-ranged force arising in polar solvents. Usually a surface force.
Solvation	Structural, epitaxial, hydration in water, depletion, hydrophobic	Either, including oscillatory	Surface force that modifies the local liquid structure.
Short-range physical	Adhesive, cohesive, surface tension, wetting, capillary	Usually attractive	Can be either a body or surface force.
Short-range chemical	Covalent, quantum mechanical, metallic, exchange, steric, hard core, Born	Ultimately repulsive at small distances	Strong, short-ranged surface forces, largely independent of the suspending liquid medium.

Table 1 lists the most common forces encountered between citrate-capped AgNPs and extended surfaces interacting in water and also summarizes the particular features of the different interactions[7]. Classical Derjaguin-Laudau-Verwey-Overbeck (DLVO) theory has been widely employed in colloid science to study particle-particle interactions and colloidal stability. This theory is based on the idea of pairwise interaction forces that arise from the interplay of attractive van der Waals forces, F_{attr}, and repulsive Coulomb forces, F_{rep}. The total interaction potential is usually hundreds or thousands of times larger than the particle kinetic energy ($mv^2/2=k_BT/2$) of Brownian motion. Obviously, the

dispersed colloid is stable for $F_{rep}>>F_{attr}$, whereas the condition of $F_{rep}<<F_{attr}$ leads to aggregation.

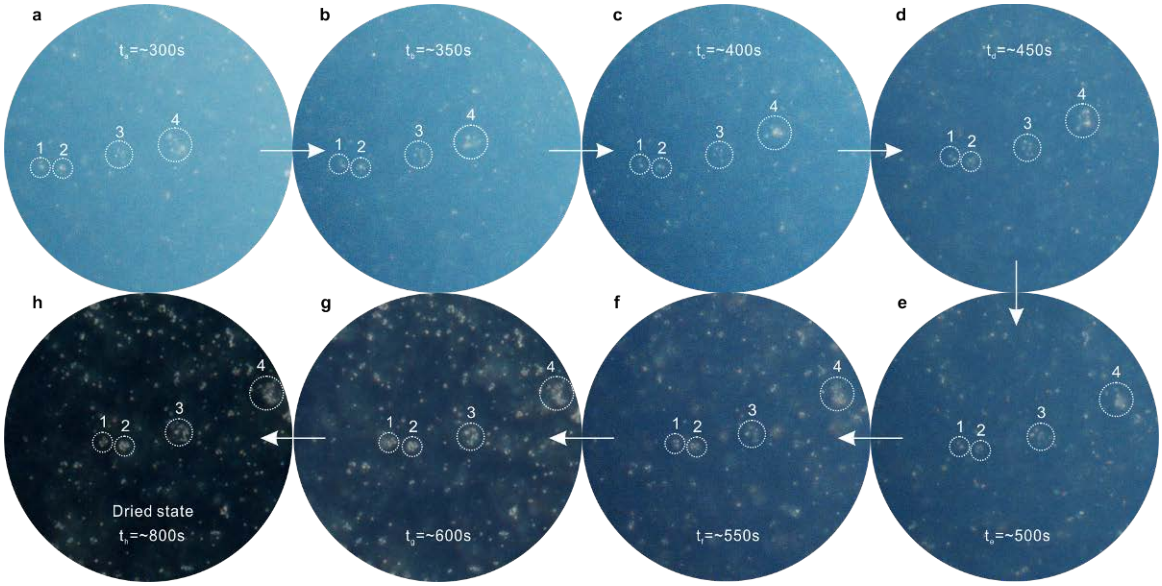

Figure S8. Dark-field optical microscopy for simultaneous tracing of the morphological alterations of four aggregates in the evaporation process of a 1-μL sample. This sample of Ag sols was 10-fold diluted with 0.01-mM citrate solution to avoid overly strong light scattering.

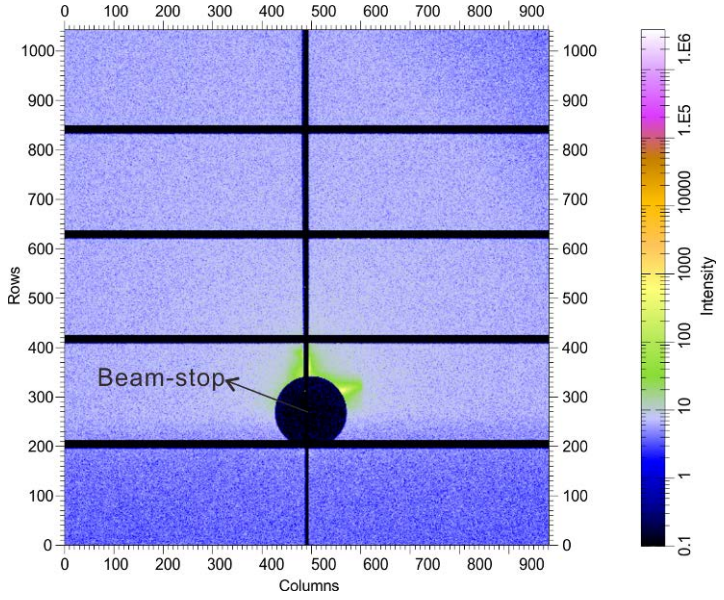

Figure S9. 2D SAXS pattern acquired from a pure quartz slide. The center black spot was produced by the beam stop used to protect the CCD detector. The background scattering of the quartz slide is rather weak compared with the scattering of the Ag nanoparticles.

S3.4. Estimation of colloidal stability in the late-stage evaporation process

When the average interparticle gap g in the droplet decreased to 2 nm, we hypothesized that the evaporation process had stopped. Here, we estimate the energy barrier ΔV required to guarantee the

particle stability of this system for a period of one hour. The mean Brownian velocity, *v*, per particle is given by

$$\frac{1}{2}mv^2 \approx \frac{1}{2}k_B T \quad (8)$$

where m=6.845×10^{-19} kg is the mass of an Ag particle (assuming a diameter of 50 nm)[3]. Thus, we obtain

$$v = \sqrt{\frac{k_B T}{m}} = 0.078 m/s \quad (9)$$

The average interparticle gap is 2 nm. Thus, the time between collisions will be approximately

$$\tau_{g=2nm} = \frac{2\times10^{-9} m}{0.0775 m/s} = 2.58\times10^{-8} s \quad (10)$$

and the number of collisions per hour will be 3600/2.58×10^{-8}=1.395×10^{11}. We therefore require that the probability (p) of two colliding particles overcoming their energy barrier ΔV should be less than 1/1.395×10^{11}=7.17×10^{-12}. In accordance with[7]

$$p = e^{-\Delta V/k_B T} < 7.17\times10^{-12} \quad (11)$$

we find

$$\Delta V \geq 26 k_B T \quad (12)$$

Thus, the energy barrier should be in excess of approximately 30$k_B T$ to ensure kinetic stability. As illustrated in Fig. 1b-II, ΔV_M is larger than 400$k_B T$ when I=0.06 M; thus, most particles remain dispersed over a period of 1 h if the evaporation process and adhesive-force effects are neglected. It should be noted that the preceding approach is known as the "ballistic" approach; a more rigorous calculation indicates that the collision rate would be significantly lower and that a much smaller energy barrier is necessary to keep the system stable.

S3.5. 3D Monte Carlo simulation of the number of hotspots

The number of "hotspots" formed among Ag particles was calculated using the Monte Carlo method (MCM), which relies on repeated random sampling to obtain numerical results. In all calculations, the diameter of the Ag nanoparticles was 50 nm, and the p-polarized plane wave had a wavelength of 532 nm. The refractive index of the surrounding medium was set to 1.33. The optical constant used for Ag was obtained from the experimental data.

S3.6. Finite element method simulation of electric-field distributions

The finite element method (FEM) was also introduced to calculate the electric-field distributions of Ag particles distributed randomly in 3D space using commercial software (Comsol Multiphysics, V4.3b). To obtain precise results, perfectly matched layer (PML) and scattering boundary conditions and a grid size of 2 nm for the Ag nanoparticles were used in our simulations.

S3.7. Optical-trapping effects

In Ag sols, R6G molecules have a tendency to migrate toward the particle surface until adsorption equilibrium is established. On the basis of measured adsorption isotherms[4], it has been estimated that approximately 80% of R6G molecules are adsorbed on Ag particles[8]; therefore, 20% of the R6G molecules are present in the solvent.

With regard to the tremendous electric-field gradients that exist at the junctions of 3D hotspot matrices, optical trapping of molecules is suspected that is analogous to the optically biased diffusion of R6G in solution, as studied via confocal fluorescence microscopy[9]. The "dipole gradient force," denoted by U, is responsible for optical trapping. The condition for the stable trapping of a molecule or particle is $U>>k_BT$. D. Klenerman et al. have estimated that the trapping potential for R6G approximately 0.08 eV/mW in nanoparticle-free aqueous solution, given an experimental temperature of T=293 K. In our system, the local electric field induced at the junction is estimated to be approximately 200 μW × (1 nm/1 μm)^2 × 10^8 = 20 mW (= laser power at the sample in Φ1 μm × relative area of the junction × enhancement factor). A trapping potential of approximately 1.6 eV is calculated at the junction by assuming the same parameters as in solution, which is comparable to a thermal energy (k_BT) of 0.026 eV at room temperature. Moreover, as predicted by theoretical simulations for surface-plasmon-enhanced optical forces[10], a trapping potential of approximately 0.3 k_BT/(mWμm^{-2}) has been obtained for R6G at the junction of two touching Ag particles of 45 nm in diameter at λ=540 nm (see Figure 1c in ref [10]). In other words, the trapping energy is approximately three times larger than the thermal energy under our experimental conditions[9].

Assuming physical adsorption of an individual R6G molecule on an Ag particle, the binding energy is comparable to the thermal energy[11]. Hence, the optical-trapping effect may induce some degree of cessation of the Brownian motion of the molecule, and R6G molecules are very likely to become trapped in the 3D hotspot matrix. Such effects could play an important role in SERS measurements and contribute to a surprising level of sensitivity beyond single-molecule detection. These aspects of optical forces have only begun to be explored and have only been reported in a small number of situations[3]; our experimental data regarding the 3D hotspot matrix might serve as an excellent example of the utilization of optical-trapping effects in SERS measurements, even though the true situation is much more complicated.

S4. 3D hotspot matrix for the detection of single molecules of R6G

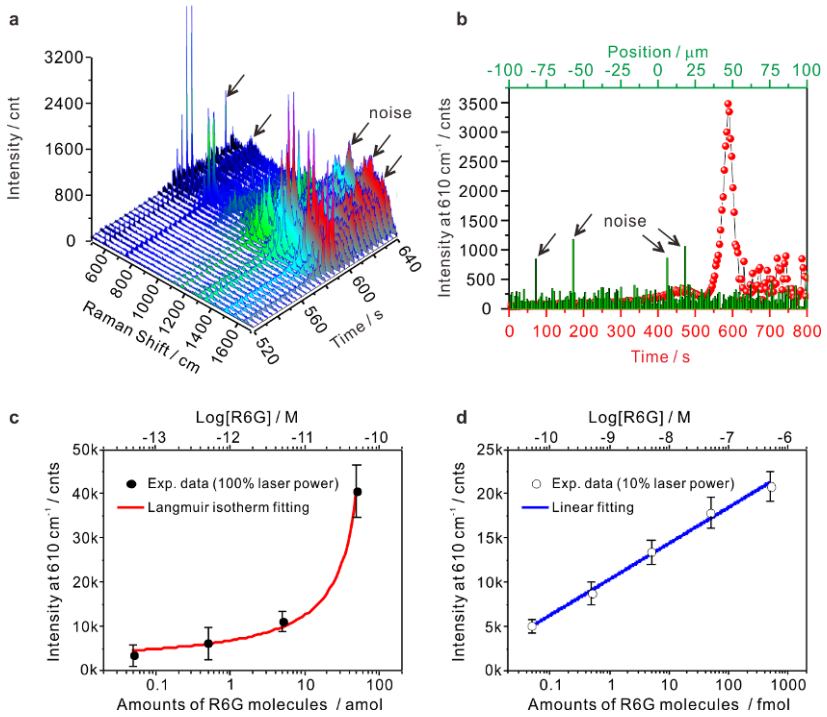

Figure S10. a, Time-course SERS mapping of a 1-μl droplet of a sample containing 0.5 amol of R6G. The peaks indicated as noise are of relatively large intensity, but their frequencies are significantly different from R6G fingerprints. **b**, The data indicated by the solid circles show the time evolution of the intensity of the 610 cm^{-1} peak during the evaporation process for 0.5 amol of R6G; the data indicated by the histogram show the intensity of the 610 cm^{-1} peak in the SERS line mapping of the dried sample in a range of -100~100 μm for 5 amol of R6G. Some 610 cm^{-1} peaks in the line mapping were considered to be noise because no other R6G fingerprints appear in these spectra, which have very low signal-to-noise ratios. **c**, SERS intensity at 610 cm^{-1} for various amounts of R6G from 0.05 amol to 50 amol. The solid curve represents the Langmuir isotherm fit to the experimental data, which were collected under 100% laser power. **d**, SERS intensity at 610 cm^{-1} for various amounts of R6G from 50 amol to 0.5 nmol. The solid curve represents the linear fit to the experimental data, which were collected under 10% laser power because saturation of the CCD detector occurs at 60k cnts. All error bars, which indicate the standard deviations of the maximum intensity of the 610 cm^{-1} peak, were obtained from at least three repeated experiments.

S5. Supplementary videos

Video I shows the time-course SERS mapping of a droplet of a sample containing 50 amol of R6G and simultaneously displays the light spots scattered onto a paper that reflect the motion of the particles in the droplet. (AVI file, 7.3 MB)

Video II shows the SERS line mapping of the dried sample. (AVI, 7.7 MB)

Abbreviations and symbols

A_H	Hamaker constant
a	side length of the imaginary cubic water shell around each Ag particle, $a=R+g$
d	diameter of the deposition area of a sample droplet
e	electron charge
g	interparticle gap between two colloidal particle surfaces
g_0	gravitational acceleration
h	droplet height of the sample
I	ionic strength of the solution
I_0	initial ionic strength of a droplet of Ag sols
k_B	Boltzmann constant
L	capillary length
m	mass of a single Ag particle
n	number of layers of deposited Ag particles
N_A	Avogadro's number
p	probability of two colliding particles overcoming their energy barrier ΔV
r_1, r_2	curvature radii
r	radius of a Ag particle
R	diameter of a Ag particle
T	absolute temperature
V_0	initial volume of a droplet of Ag sols
V_g	droplet volume for an average interparticle gap g
V_E	electrostatic repulsion potential
V_V	van der Waals attraction potential
V_T	total interaction potential
γ	surface tension between air and liquid
ΔP	pressure difference between liquid and air
ΔV	energy barrier
ΔV_M	maximum energy barrier
ε_0	dielectric permittivity in vacuum
ε_r	relative dielectric permittivity of the water (approximately 80 at 298 K)
θ	wetting angle
κ	inverse Debye length
κ^{-1}	thickness of the diffuse layer around the AgNPs
λ	characteristic wavelength of interaction (taken to be 100 nm)
v	mean Brownian velocity of Ag particles in a water droplet
ρ	mass density of a liquid
τ	time interval between two particle collisions
Φ	diameter of the laser spot
ψ_0	particle surface potential

References

1. Ilavsky, J. & Jemian, P.R. Irena: tool suite for modeling and analysis of small-angle scattering. *J Appl Crystallogr* **42**, 347-353 (2009).
2. Lee, P.C. & Meisel, D. Adsorption and Surface-Enhanced Raman of Dyes on Silver and Gold Sols. *J Phys Chem-Us* **86**, 3391-3395 (1982).
3. Eric C. Le Ru & Etchegoin, P.G. Principles of surface-enhanced Raman spectroscopy. (Elsevier, 2009).
4. Hildebrandt, P. & Stockburger, M. Surface-Enhanced Resonance Raman-Spectroscopy of Rhodamine-6g Adsorbed on Colloidal Silver. *J Phys Chem-Us* **88**, 5935-5944 (1984).
5. Yunker, P.J., Still, T., Lohr, M.A. & Yodh, A.G. Suppression of the coffee-ring effect by shape-dependent capillary interactions. *Nature* **476**, 308-311 (2011).
6. Mitarai, N. & Nori, F. Wet granular materials. *Adv. Phys.* **55**, 1-45 (2006).
7. Israelachvili, J.N. Intermolecular and Surface Forces, Edn. Third edition. (Academic Press, Elsevier, London; 2011).
8. Nie, S.M. & Emery, S.R. Probing single molecules and single nanoparticles by surface-enhanced Raman scattering. *Science* **275**, 1102-1106 (1997).
9. Osborne, M.A., Balasubramanian, S., Furey, W.S. & Klenerman, D. Optically biased diffusion of single molecules studied by confocal fluorescence microscopy. *J. Phys. Chem. B* **102**, 3160-3167 (1998).
10. Xu, H.X. & Kall, M. Surface-plasmon-enhanced optical forces in silver nanoaggregates. *Physical Review Letters* **89** (2002).
11. Maruyama, Y., Ishikawa, M. & Futamata, M. Thermal activation of blinking in SERS signal. *J. Phys. Chem. B* **108**, 673-678 (2004).